Electronic supplementary information

Lithographically Patterned Well-Type Graphene Liquid Cell with Rational Design

Namgyu Noh,[a] *Jungjae Park,*[a] *Ji Su Park,*[a] *Kunmo Koo,*[a] *Jae Yeol Park,*[a] *and Jong Min Yuk*,*[a]

[a]Department of Materials Science & Engineering, Korea Advanced Institute of Science and Technology (KAIST), 291 Daehak-ro, Yuseong-gu, Daejeon, 34141, Republic of Korea,

*Corresponding author. Email: jongmin.yuk@kaist.ac.kr
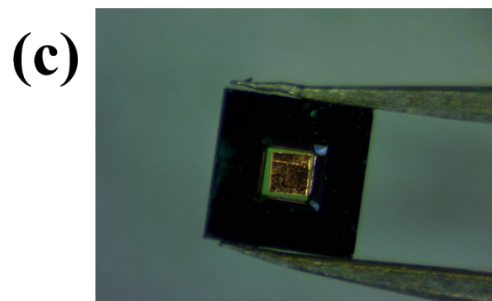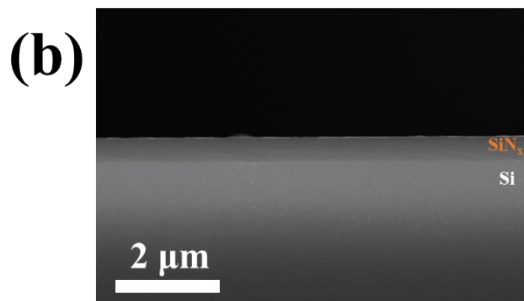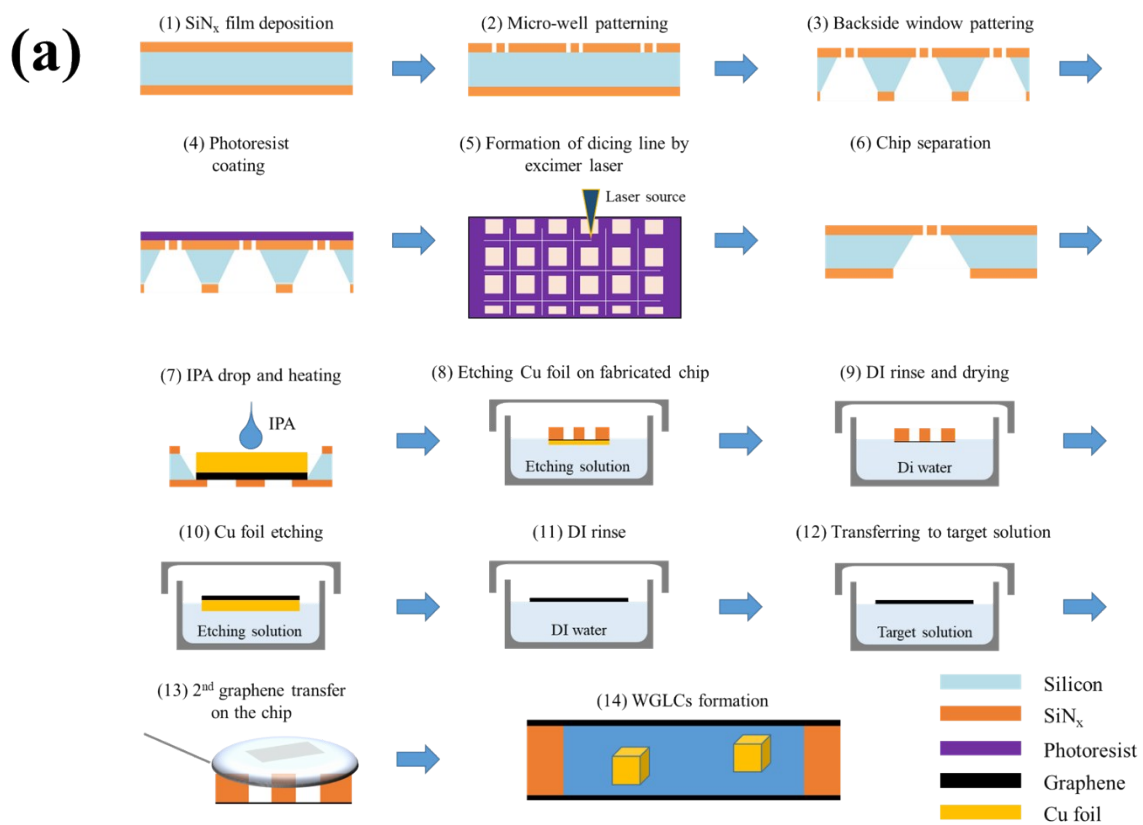
Fig. S1 (a) The schematics of detailed fabrication process for formation of WGLCs. (b) the cross section SEM image of deposited SiN$_x$ film onto Si wafer. A 500 nm thick SiN$_x$ film is directly formed onto silicon wafer without either surface or internal crack. (c) OM image of the Cu foil with graphene placed on the bottom membrane of the chip.
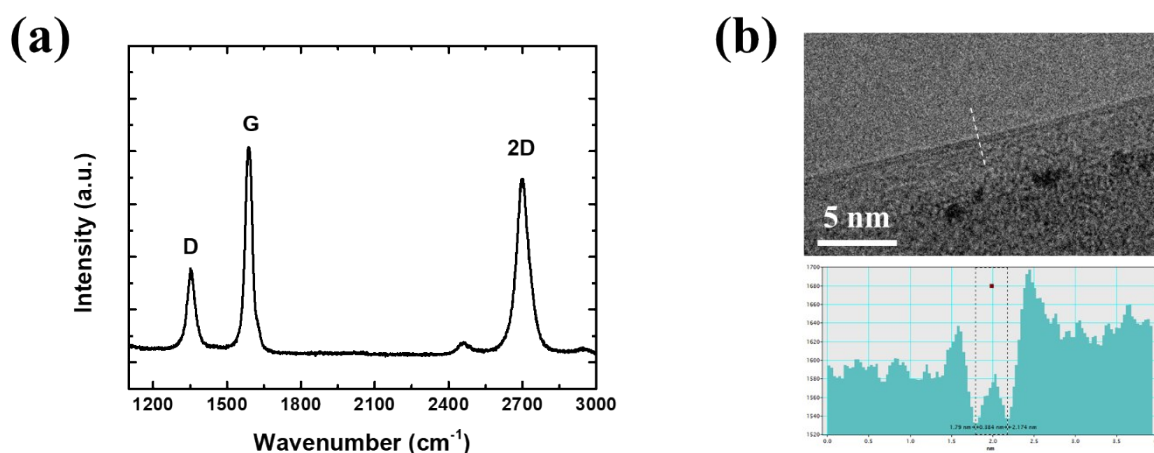
Fig. S2 (a) Optical characterization of CVD graphene. Raman spectra of multilayer graphene transferred on SiO$_2$ substrate. (b) HRTEM image and intensity profile of CVD grown graphene at the edge of folded graphene.

To characterize the CVD graphene grown on the Cu foil, we perform Raman and TEM analysis. The Raman was measured using Raman spectroscopy (ARAMIS, Horiba) under laser wavelength of 514 nm and TEM observation of CVD graphene was performed utilizing JEOL 3010 TEM. For the Raman and TEM analysis, we prepared samples with the graphene transferred onto SiO$_2$/Si substrate and onto TEM grid, respectively. In Raman analysis, the spectrum of graphene clearly shows the graphene characteristic peaks which are related to D, G and 2D peak at 1350 cm^{-1}, 1587 cm^{-1} and 2701 cm^{-1}, respectively (Fig. S2a). The 2D/G ratio of Raman signature of CVD graphene is 1.17 which corresponded to a bilayer graphene. In the fig. S2b shows cross section image at the edge of a folded graphene region. The HRTEM image of the graphene reveals the two carbon layers. From these results, we determined that our CVD grown graphene is a bilayer film.
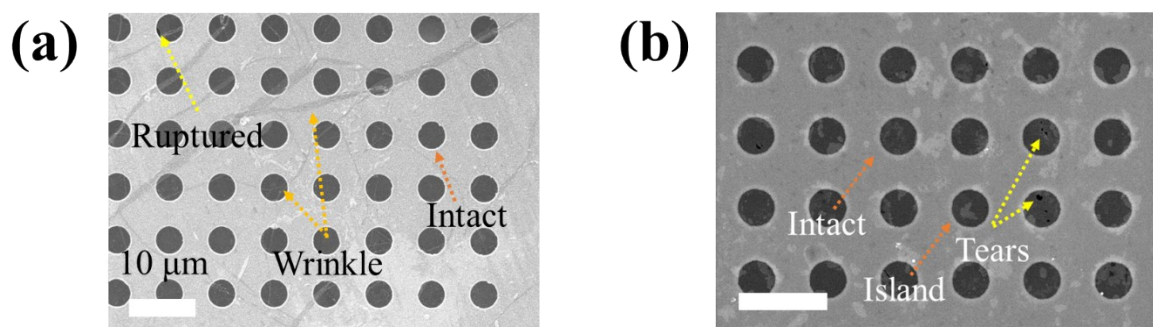
Fig. S3 The morphology analysis of the transferred graphene by using SEM. (a) The SEM image of graphene transferred by loop transfer onto the top of the chip. (b) The SEM image of graphene transferred by direct transfer onto the bottom of the chip.

SEM images show the top and bottom graphene transferred on the perforated film. Depending on the transfer method, the transferred graphene has different morphology and yield. The top and bottom graphene contain the intact region as well as wrinkle and ruptured region in the hole. The yield of the top and bottom graphene is above 90% and 80 %, respectively, and the typical yield of fabricated WGLCs is about 64 % except for precipitated salt area.
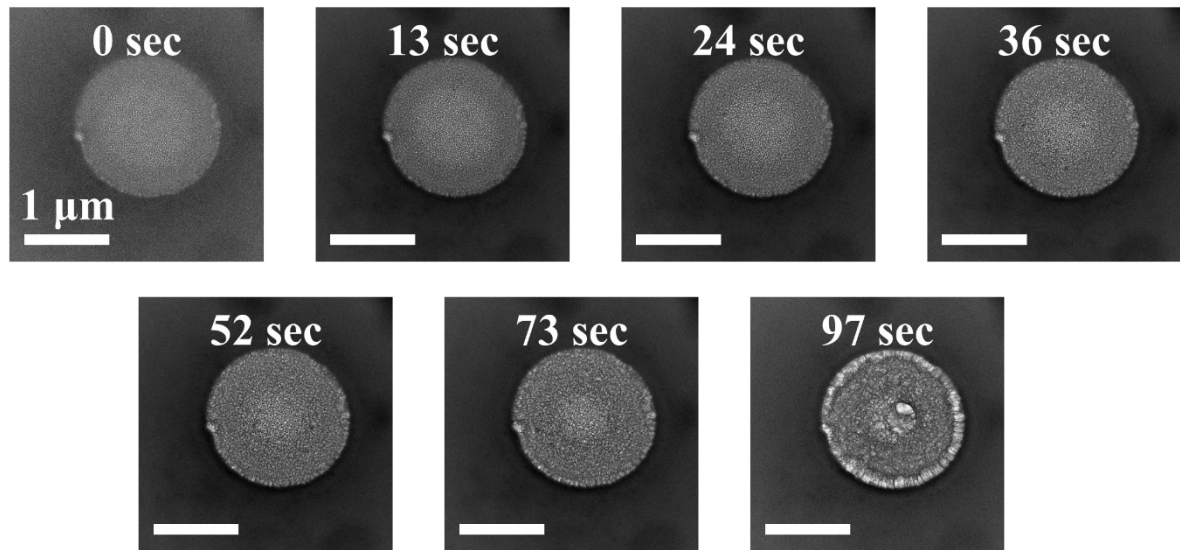
Fig. S4 The time series TEM images of bubble generated in fully trapped WGLC during electron beam exposure.

In order to confirm the liquid trapped in the well, we investigate the bubble formation in the WGLCs. For the TEM imaging, the liquid can generate gases species, such as H_3O+, H, OH, H_2 and H_2O_2, under the accelerated electron beam condition.[1,2] . For imaging of bubbles, the TEM observation was carried out by JEM 2100F equipped with OneView camera at an accelerated voltage of 200 kV and the electron dose maintained higher than the required dose for bubble generation [ref]. The TEM images of trapped target solution in the hole pattern contain many bubbles, which have a circular shape-like bright contrast due to low inelastic scattering of transmitted electron [3]. At relatively low electron dose condition from 0 sec to 73 sec, bubbles with nanometer size are formed in the whole area of the well and the nanobubbles is very slowly grown from primary bubbles in imaging condition. At high dose condition after 73 sec, bubbles is fast grown and coalescence between bubbles is mainly occurred near the edge of the wall. The large bubbles in the center region at 97 sec are instantaneously formed by focused beam. Furthermore, some of the WGLCs, which is located right beside the viewing area, already contain bubbles since the difference in viewing area of the detector and the beam exposure area.
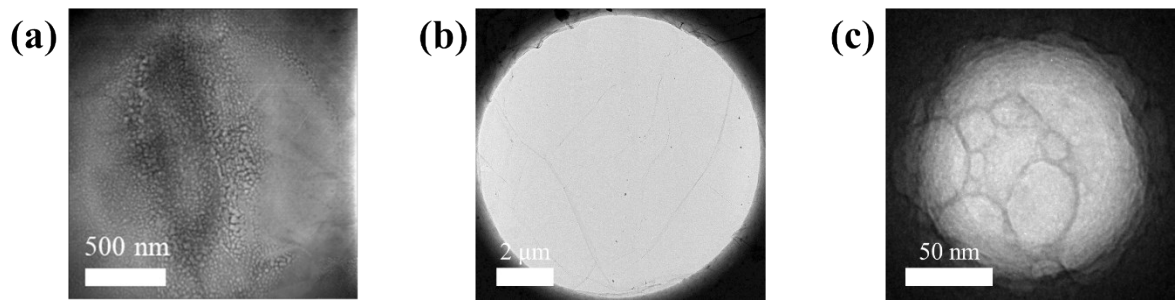
Fig. S5 TEM images of WGLC with various well dimension. Spacer thickness and hole diameter of WGLCs is (a) 150 nm and 1.5 μm (ring type) (b) 150 nm and 10 μm (none type), and (c) 200 nm and 200 nm (full type), respectively.
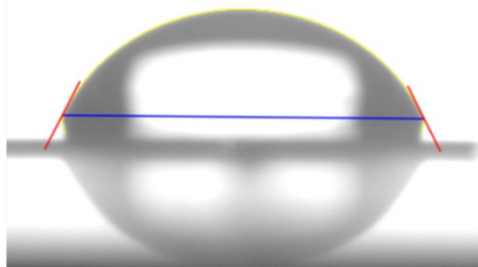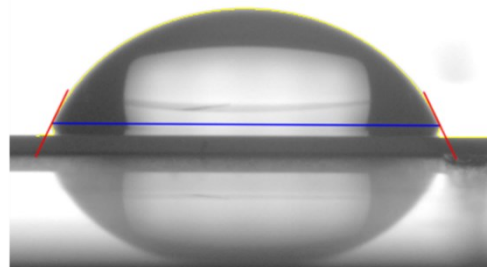
Fig. S6 Contact angle of (a) DI water and (b) 0.1M PBS solution on 150 nm thickness SiN$_x$ film is 64.36 ° and 64.85 °, respectively.

The contact angle was measured by contact angle analyzer (SEO phoenix) in static condition using drop method. Before the contact angle measurement, a SiN$_x$ film was prepared by standard cleaning process using acetone and IPA. Then, the DI water and 0.1M PBS solution was dropped onto the SiN$_x$ film and the contact angle was immediately measured.
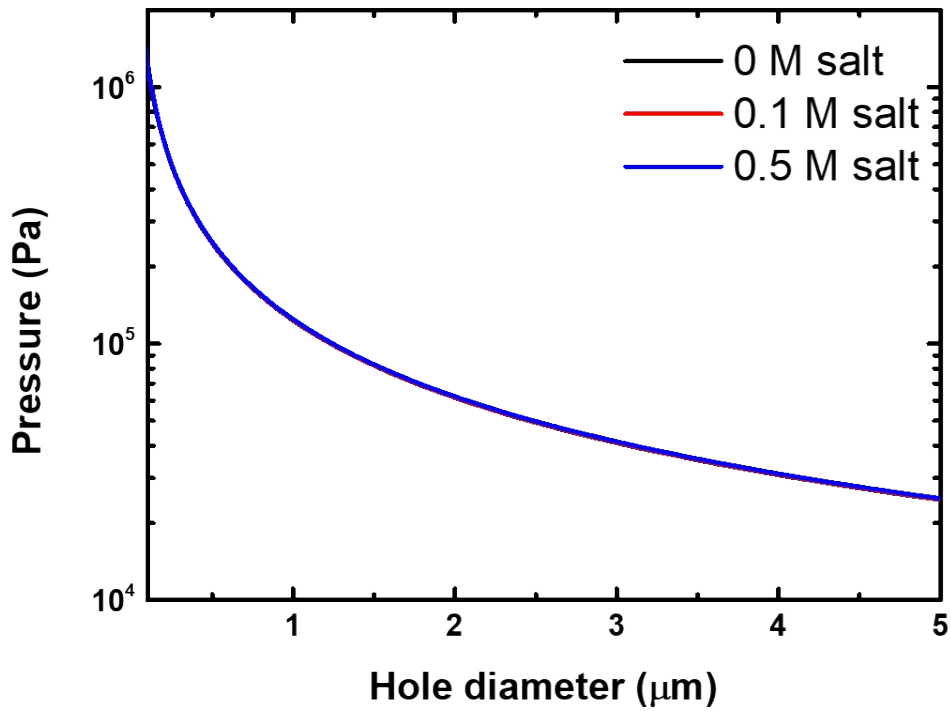
Fig. S7 Calculation results of (a) capillary pressure as function of hole diameter and salt concentration in DI water.

   The liquid in the well structure has the meniscus for minimization of surface energy. This behavior can describe the capillary pressure, P_{cap}, which is generally given by

$$P_{cap} = \frac{4\gamma^{liquid}cos\theta}{d}$$

....(S1)

where the γ^{liquid} is surface tension of liquid, the θ is contact angle between liquid and SiN_x spacer and d is hole diameter.[4] For target solution, we calculate the capillary pressure as NaCl concentration and hole diameter. In fig. S7, the capillary pressure of target solution is determined by relative surface tension of 0.1 M salt and 0.5 M salt, which is 0.0730 N/m and 0.0737 N/m, respectively [5].

(a)

(b)
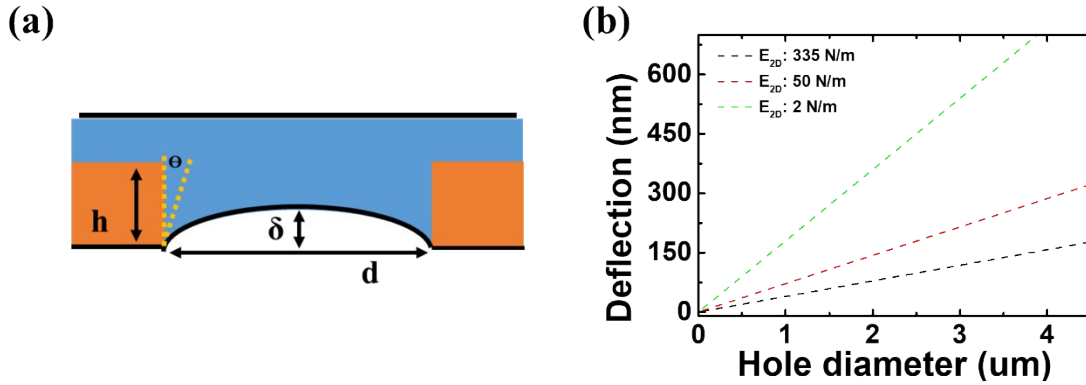
Fig. S8 (a) A schematic for deflection of clamped bottom graphene in WGLC (b) The results of graphene deflection as a function of hole diameter calculated from equation S3.

To explain the graphene bending in WGLC, we consider capillary pressure and graphene bowing related to the trapped liquid in circular cavity. The pressure generated by the liquid surface can be described by equation S1. We assume that this capillary pressure is typically applied onto the suspended graphene surface The pressurized thin membrane can be described by modified Hencky's equation with pretension in membrane.[6–8] This solution provides the information about central deflection of clamped circular membrane under the hydrostatic pressure.

$$P = \frac{4\sigma}{d^2}\delta + \frac{16E_{2D}q^3}{\pi d^4}\delta^3$$ ....(S2)

Here P is a applied pressure to membrane, δ is maximum deflection at center of the hole, σ is pretention of graphene membrane (0.0838 N/m) [7,9], E_{2D} is Young's modulus of 2D materials (335 N/m) [6] and q is dimensionless constant 1.02 calculated Poisson's ratio of the graphene, $v = 0.165$ [6]. Thus, the deflection of suspended 2D materials by capillary pressure in liquid cell is rewritten;

$$\gamma^{liquid}cos\theta = \frac{\sigma}{d}\delta + \frac{4E_{2D}q^3}{\pi d^3}\delta^3$$ ....(S3)

The equation S3 is simply induced by combination of equation S1 and equation S2. In our design, the calculated capillary pressure has a few tens of kPa range. Under the pressure, the bowing of the membrane increases as the hole diameter increase. For ideal flat graphene, the central deflection of membrane is 78 nm and 157 nm at 2 μm and 4 μm hole diameter, respectively. As decreasing E_{2D}, the bowing of graphene increases ~ 2 times (E_{2D}: 50 N/m) and ~ 4.5 times (E_{2D}: 2 N/m) larger than the

expected value of flat graphene at 2 μm hole diameter, respectively.
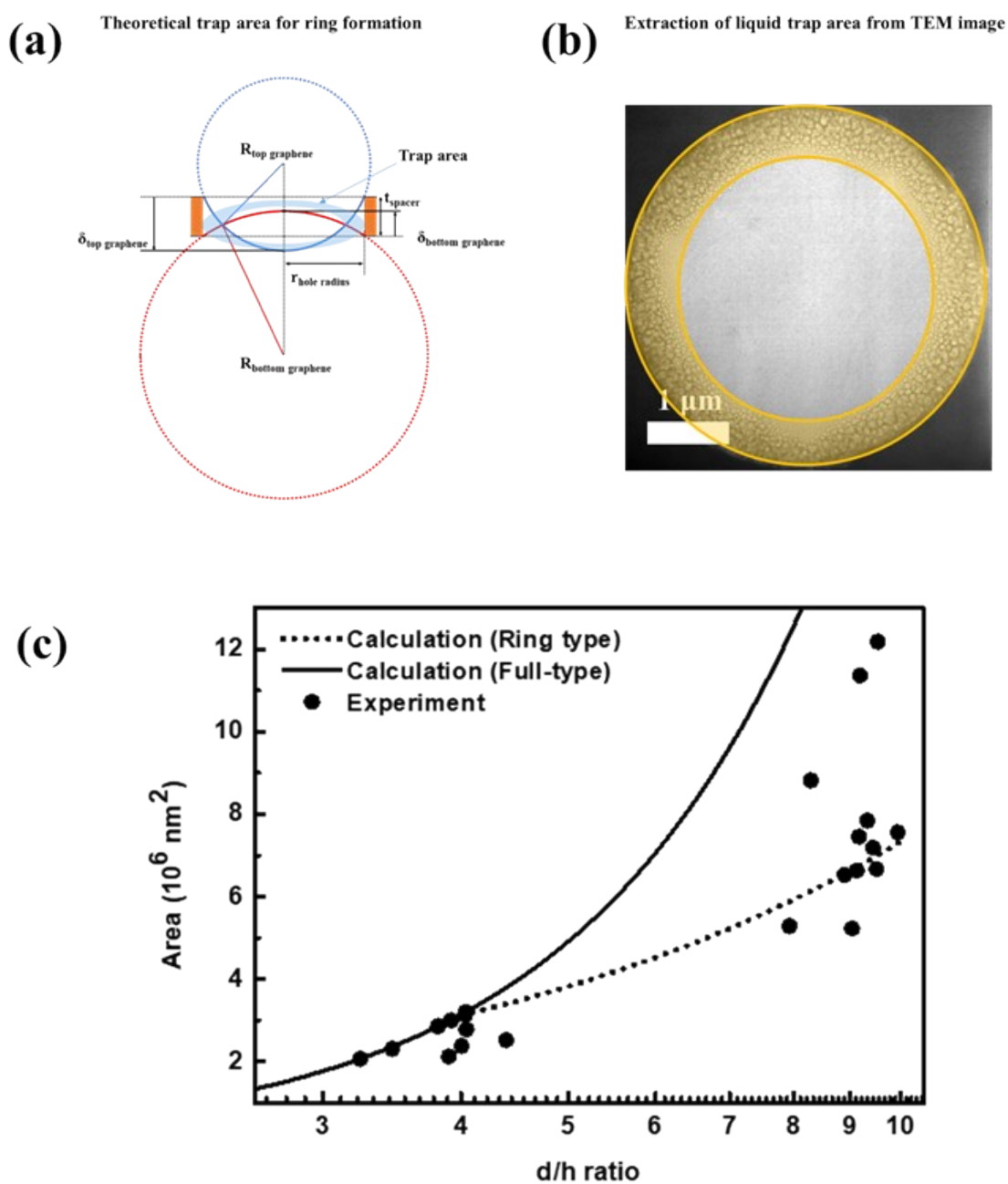
Fig. S9 Extraction model of (a) theoretical and (b) experimental projection area of trapped liquid. (c) The comparison of liquid trap areas of calculated and experiment data in WGLCs. Dashed and solid line is calculation results of ring type and full type, respectively. Spheres depict the projection area of trapped liquid extracted from individual TEM images.

For evaluating the correlation between experimental and our hypothesis on trapped liquid and graphene bending, we consider the projection area of trapped liquid region with calculation and

experimental results. The area of trapped liquid in the well is depending on the bending behavior of the top and bottom graphene by capillary pressure of liquid and it can be induced by intersection of top and bottom graphene. The graphene bended by capillary pressure can be approximated by partial region of surface of a sphere (Fig. S9a). The intersection of two graphene membranes can be changed by deflection of hole diameter calculated by equation 3 and it is also directly correlated to the hole diameter. Following the given approximation, we carry out the calculation about intersection of the top and bottom graphene. Using the values corresponding to the calculated deflection of top and bottom graphene ($\delta_{top\ graphene}$ and $\delta_{bottom\ graphene}$ shown in fig. S8b) and the liquid cell design (hole radius, $r_{hole\ radius}$ and spacer thickness, t_{spacer}), we calculate the radius of top ($R_{top\ graphene}$) and bottom ($R_{top\ graphene}$) graphene and compute the expected trap area from the intersection calculated by radius of top and bottom graphene. And also, using the TEM image of fabricated WGLCs, we extract a projection area of the trapped liquid region (Fig. S9b) of 24 different liquid cell region.

The Fig. S9c shows that calculation line of trap area of ring type WGLC is located lower than the full-type WGLC. The most of the experimental data follows the ring type line upper transition point of WGLCs with 4 of d/h ratio. From a few samples, we observe a large trapped area compared to calculation line of ring type at high d/h ratio which is reflected by increase of trap area of liquid by formation of micro wrinkles. From this results, we confirm the high coherency between trapped liquid area of calculation and experiment in WGLC.
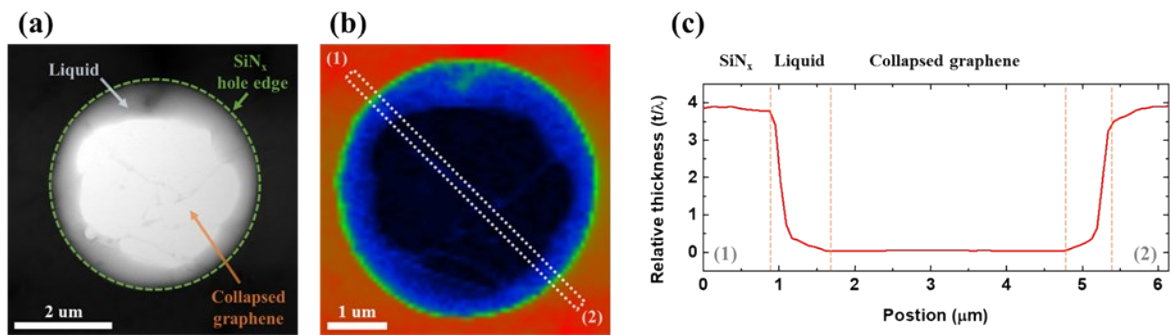
Fig. S10 Thickness characterization of WGLC as a function of relative position by using STEM-EELS measurement. (a) Bright field TEM image of ring type WGLC. (b) Relative thickness map corresponding to (a). (c) Line profile of relative thickness as position related on (1)-(2) of (b).

In order to estimate the thickness of trapped liquid in the fabricated WGLC, we performed the thickness calculation by log-ratio equation utilizing STEM-EELS measurement.[10–13] The log-ratio equation can be described by

$$\frac{I}{I_0} = exp(-\frac{t}{\lambda})$$

.... (S4)

where t is thickness of material, λ is mean-free path, I is the zero loss peak intensity and I_0 is total intensity of EELS spectrum. Utilizing STEM condition (accelerated voltage: 200 kV and convergence angle: 20 mrad), we calculate the relative thickness of spacer, liquid and collapsed graphene region from the EELS spectrum as each pixel by equation (4). The line profile of relative thickness is nearly zero at collapsed region due to absent of liquid. However, the thickness of trapped liquid region is abruptly increased from end of collapsed region to SiN_x region in the well.
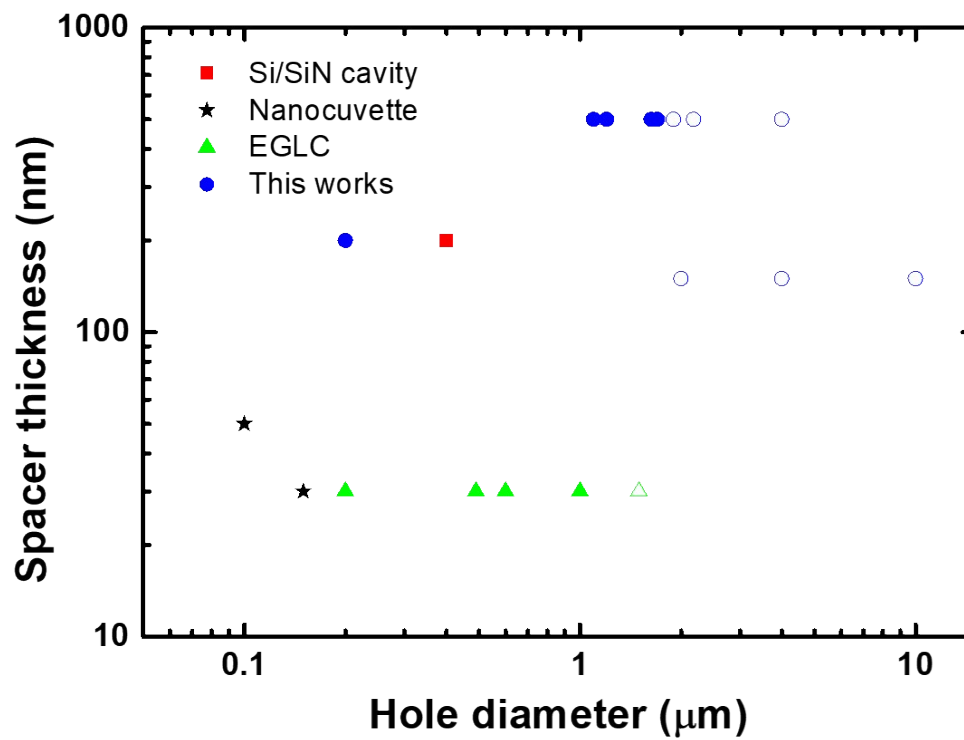
Fig. S11 Experimental results of the reported WGLC (Square: Si/SiN cavity [14], Star: nanocuvette [15], Triangle: engineering GLC (EGLC) [16], and Circle: This works). The solid points are full type and the open shape is ring or none type.
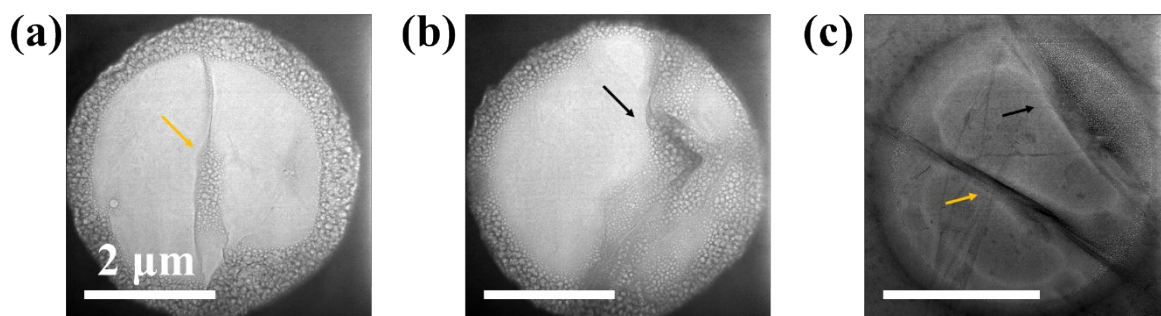
Fig. S12 TEM images of various ring type WGLC in other samples. Their trap behaviors induced by morphological defect, such as wrinkle or folding, of graphene are shown as (a) line trap, (b) half trap and (c) its combination. Yellow arrow and dark arrow is the line and half occupation area of the liquid, respectively.
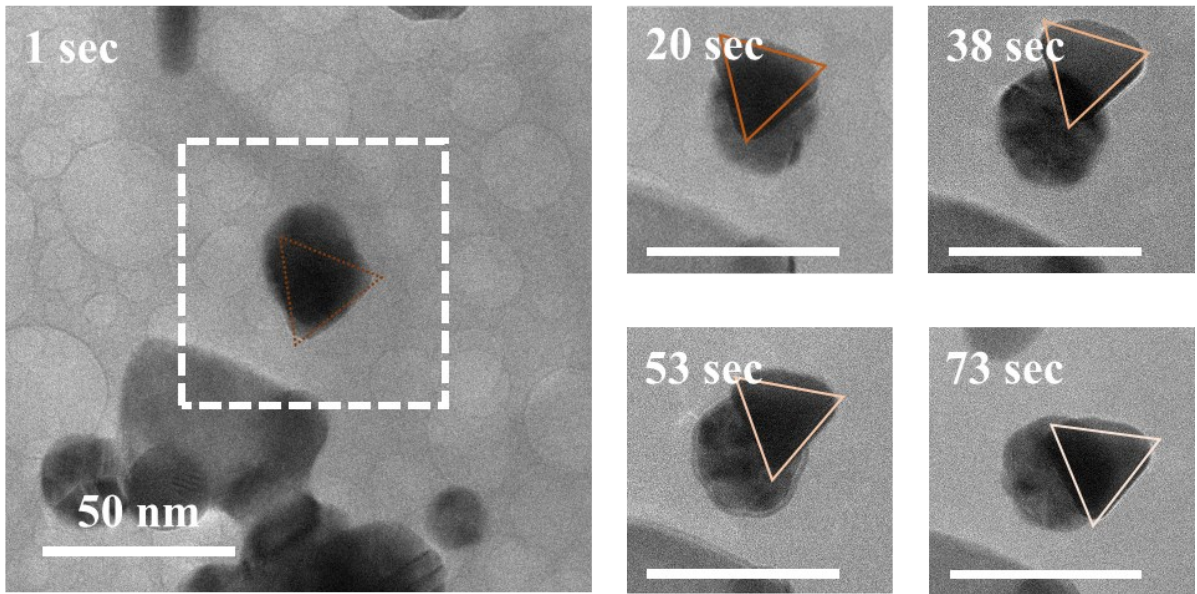
Fig. S13 Time-series TEM images of Au particles movement in WGLC.
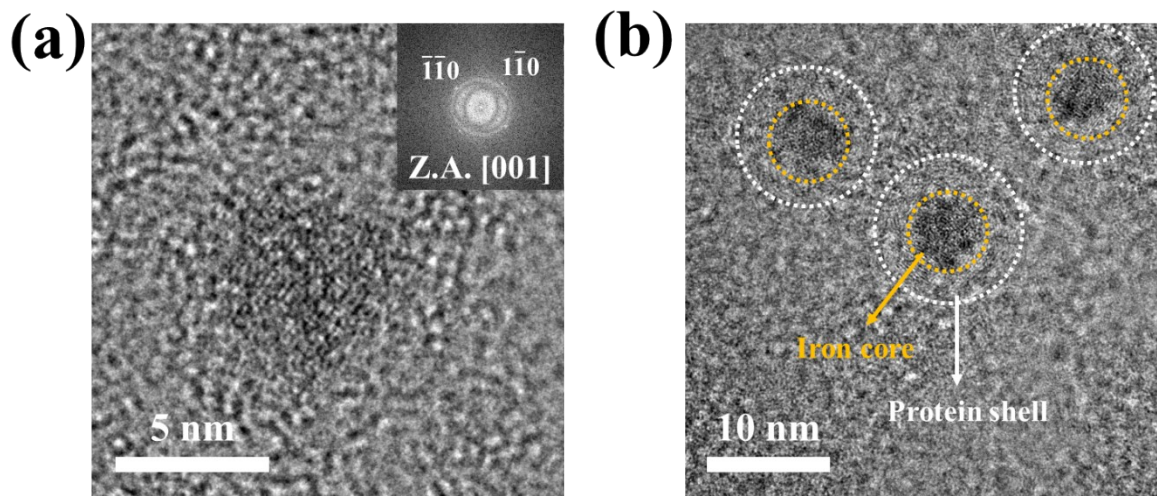
Fig. S14 Ferritin encapsulated in graphene veil structure. (a) High resolution TEM image of iron core of ferritin. The inset shows FFT pattern corresponding to (110) family of plane of iron at [001] zone axis. (b) Under-focused TEM image of ferritin. Yellow dashed circle depicts iron core region and white dashed circle depicts protein shell region.
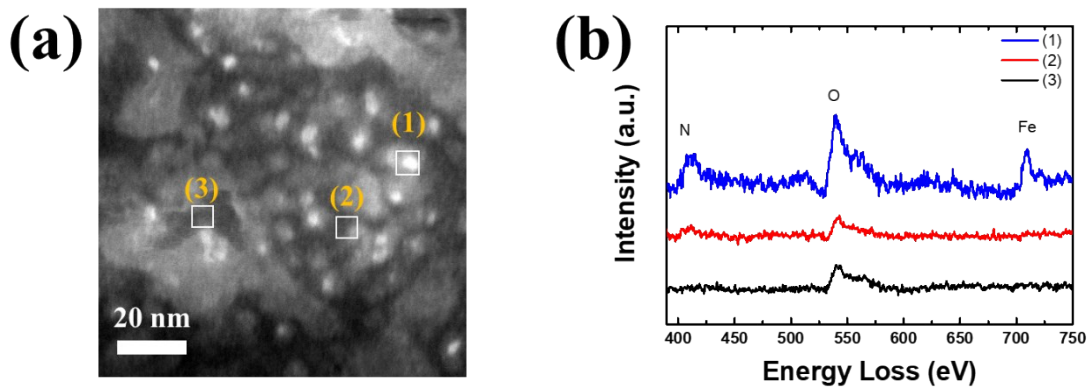
Fig. S15 (a) ADF STEM image (shown in Figure 5d) and (b) a representative EELS spectrum corresponding to (1) ferritin, (2) apoferritin, and (3) liquid area in WGLC. The N K-edge, O K-edge and Fe L-edge is located at 402 eV, 532 eV and ~710 eV, respectively.

Supplementary references

1   N. M. Schneider, M. M. Norton, B. J. Mendel, J. M. Grogan, F. M. Ross and H. H. Bau, *J. Phys. Chem. C*, 2014, **118**, 22373–22382.

2   J. M. Grogan, N. M. Schneider, F. M. Ross and H. H. Bau, *Nano Lett.*, 2014, **14**, 359–364.

3   J. M. Yuk, Q. Zhou, J. Chang, P. Ercius, A. P. Alivisatos and A. Zettl, *ACS Nano*, 2016, **10**, 88–92.

4   A. B. Tugrul, *NDT E Int.*, 1997, **30**, 19–23.

5   G. Jones and W. A. Ray, *J. Am. Chem. Soc.*, 1941, **63**, 3262–3263.

6   C. Lee, X. Wei, J. W. Kysar and J. Hone, *Science (80-.).*, 2008, **321**, 385–388.

7   C. K. Lee, Y. Hwangbo, S. M. Kim, S. K. Lee, S. M. Lee, S. S. Kim, K. S. Kim, H. J. Lee, B. I. Choi, C. K. Song, J. H. Ahn and J. H. Kim, *ACS Nano*, 2014, **8**, 2336–2344.

8   K. T. Wan, S. Guo and D. A. Dillard, *Thin Solid Films*, 2003, **425**, 150–162.

9   C. S. Ruiz-Vargas, H. L. Zhuang, P. Y. Huang, A. M. Van Der Zande, S. Garg, P. L. McEuen, D. A. Muller, R. G. Hennig and J. Park, *Nano Lett.*, 2011, **11**, 2259–2263.

10   E. M. Technique, S. Cheng, L. Berkeley and N. Labor, , DOI:10.1002/jemt.1060080206.

11   U. Mirsaidov, C.-D. Ohl and P. Matsudaira, *Soft Matter*, 2012, **8**, 7108.

12   K. L. Jungjohann, J. E. Evans, J. A. Aguiar, I. Arslan and N. D. Browning, *Microsc. Microanal.*, 2012, **18**, 621–627.

13   M. E. Holtz, Y. Yu, J. Gao, H. D. Abruña and D. A. Muller, *Microsc. Microanal.*, 2013, **19**, 1027–1035.

14   H. Rasool, G. Dunn, A. Fathalizadeh and A. Zettl, *Phys. status solidi B*, 2016, **253**, 2351–2354.

15   C. Wadell, S. Inagaki, T. Nakamura, J. Shi, Y. Nakamura and T. Sannomiya, *ACS Nano*, 2017, **11**, 1264–1272.

16   D. J. Kelly, M. Zhou, N. Clark, M. J. Hamer, E. A. Lewis, A. M. Rakowski, S. J. Haigh and R. V Gorbachev, *Nano Lett.*, 2018, **18**, 1168–1174.